

COMPARISON OF ACOUSTIC AND ELASTIC FULL-WAVEFORM INVERSION OF 2D TOWED-STREAMER DATA IN THE PRESENCE OF SALT

N. Thiel, T. Hertweck and T. Bohlen

email: *Niklas.Thiel@kit.edu, Thomas.Hertweck@kit.edu*

keywords: *Acoustics, Elastics, Full waveform, Inversion, Seismics*

ABSTRACT

Over the last years full-waveform inversion (FWI) has become an important tool in the list of processing and imaging technologies available to the industry. For marine towed-streamer data, FWI is typically applied using an acoustic approximation because S-waves do not propagate in water and elastic effects in recorded data are generally assumed to be small. We compare acoustic and elastic modelling and FWI for a field data set acquired offshore Angola over sediments containing a salt body with significant topology. Forward modelling tests reveal that such geological structures lead to significant mode conversions at interfaces and, consequently, to significant relative amplitude differences when elastically and acoustically modelled traces are compared. Using an acoustic approach for modelling in FWI therefore leads to problems matching the synthetic data with the field data, even for recorded pressure data and with trace normalisation applied. FWI is unable to find consistent model updates. Applying elastic FWI leads to more consistent and reliable model updates with less artefacts, at the expense of additional computation cost. Although 2D marine towed-streamer data are least favourable for the application of FWI compared to 3D data or ocean-bottom data, it is recommended to check on the existence of elastic effects before deciding on the final processing and imaging approach.

INTRODUCTION

Over the last years we have seen the industry move toward full-wavefield imaging, employing for instance full-waveform inversion (FWI) to obtain high-resolution parameter models of the subsurface. As opposed to ray-based methods such as tomography, which often only use kinematic information of the data, FWI tries to exploit both the phase and amplitude of the seismic waveforms. Basically, it does so by comparing forward-modelled data using initial parameter models with data acquired in the field and iteratively updating the models until a good match of the two data sets is achieved. While FWI itself is not a new method (see, e.g., Tarantola, 1984), only recent advances in computer technology have made this computationally demanding method applicable to larger field data sets. In doing so, the industry typically applies an acoustic approximation, at least for marine towed-streamer data, which requires two initial parameter models, namely the P-wave velocity (v_P) and the density (ρ). In this work we compare such an approach with elastic FWI where in addition to aforementioned parameter models we also require the S-wave velocity (v_S). In both the acoustic and elastic approach additional wave propagation effects, such as anisotropy or attenuation, can be taken into account. However, there is a limit to the number of parameters that can reliably be inverted in practice due to, for instance, so-called cross-talk, lack of available offsets or cycle-skipping issues, to name a few. Often, only the P-wave velocity is actually inverted while other parameters are treated as passive parameters, i.e., they are subsequently deduced or kept constant throughout the process (e.g., Brossier et al., 2009).

There are various publications showing the successful application of FWI to synthetic and field data: For instance, Warner et al. (2013) describe the application of acoustic FWI on a 3D 4C ocean-bottom data set, or Xiao et al. (2016) present acoustic FWI results for a 2D broadband line acquired offshore Gabon using variable-depth streamers. An elastic FWI application on ocean-bottom field data has been shown by, e.g., Vigh et al. (2014). Most authors focus on the velocity parameters. Although the importance of density is well known (e.g., Plessix et al., 2013), only few authors were able to show a successful density inversion, even for synthetic data (Jeong et al., 2012). There are hardly any publications of elastic inversion for marine towed-streamer data; such data are often assumed to be well handled by an acoustic approximation. However, as we will show later on, this is not always the case. Köhn et al. (2012) show a synthetic, elastic study using the Marmousi-II model in a marine environment with velocity receivers. Shipp and Singh (2002) present an elastic inversion strategy for wide-aperture streamer data, but focus only on the v_P result. In another publication Lu et al. (2013) show a promising synthetic case study for an elastic FWI of marine pressure data, but no actual field data application.

In this work we examine the use of elastic FWI on a towed-streamer 2D field data set acquired over a complex salt structure, and compare the results to acoustic FWI. Our main focus is on the sediment structures above the salt and the top of salt (TOS). After explaining our FWI methodology in more detail, we present the data and initial parameter models, investigate some of their properties through forward modelling tests, and run synthetic as well as field data inversions. Finally, we draw some conclusions based on these results and comparisons. In general, elastic inversion of 2D streamer data acquired over complex geology in fairly deep water is rather challenging, as such an acquisition scenario is least favourable for a successful FWI application; there are hardly any diving waves recorded at all, even with a 10 km-long streamer. However, it may open opportunities to investigate and reprocess older 2D data sets in order to obtain additional useful information.

FWI METHODOLOGY

For the modellings and inversions shown in this study we use a 2D elastic FWI code developed by Köhn (2011). It is based on a 2D finite-difference (FD) scheme in the time domain (e.g., Tarantola, 1984). The forward modelling code was originally developed by Bohlen (2002). The propagation of elastic waves is modelled on a standard staggered grid (e.g., Virieux, 1986; Levander, 1988) in the stress-velocity formulation. Reflections at the boundaries of the model are avoided by means of convolutional perfectly matched layers (CPMLs) implemented in the code (Komatitsch and Martin, 2007; Martin and Komatitsch, 2009). In addition, a free-surface condition is applied, originally proposed by Levander (1988) and updated by Robertsson et al. (1995). This free-surface condition minimises the size of the model by avoiding the need for an additional air layer with absorbing boundary.

In order to quantify the data misfit of the field data and the modelled data, a least-squares norm of the normalised wavefields is used, as suggested by Choi and Alkhalifah (2012). The trace normalisation is applied to both, the synthetic and the field data, and reduces the effects of amplitude decay with offset produced by, e.g., geometrical spreading and anelastic effects. Together with the source wavelet inversion, this normalised L2-norm proved to be more robust for field data than the ordinary L2-norm without normalisation (Przebindowska, 2013). The normalisation does not affect time-varying relative amplitude differences within a trace. Such differences can be generated by elastic effects and 3D effects not taken into account in the modelling. In order to correct for the 3D spreading effects not considered in 2D forward modelling, a 3D-to-2D transformation, proposed by Forbriger et al. (2014), is applied to the field data. It corrects for both amplitude and phase differences between 2D and 3D wave propagation. The quality of the 3D-to-2D transformation in the context of elastic FWI of marine streamer data was investigated by Köhn (2011) using the marine elastic Marmousi2 model. It was discovered that small-scale artefacts in the reconstructed P-wave, S-wave velocity and density models at shallow depth (below seafloor) may lead to a loss of resolution. Large structures and laterally extended layers, however, are still identifiable in the reconstructions.

To ensure an accurate comparison of the field data and forward-modelled synthetic data, the determination of the source wavelet plays an important role for a successful FWI application. Pratt (1999) proposed an iterative, linear least-squares optimisation inversion for the source signature. The method is based on a deconvolution of the field data and synthetic data in the frequency domain. We use a stabilised version

of his approach in our code (see, e.g., appendix A in Groos, 2013) and denote it as source-time-function (STF) inversion throughout the paper.

For the calculation of the Fréchet derivatives, the adjoint approach is used (Tarantola, 1984; Mora, 1987; Tromp et al., 2005; Plessix, 2006). For a detailed description of how the gradients are calculated, we refer the reader to Köhn (2011). After the gradient calculation, a step length is determined. This parameter scales the update of the model. We use a parabolic line-search method as proposed by Nocedal and Wright (1999). Before the actual update is performed, the gradients are weighted (masked); for instance, in our examples the water column was assumed to be known and not updated in FWI. Thus, acquisition footprints can largely be prevented in the inverted models (Thiel, 2018).

In order to avoid cycle-skipping as best as possible, a multiscale approach is used as described by, e.g., Bunks et al. (1995). Non-linearities are reduced by starting with low frequencies and gradually increasing the frequency content of the inverted data. We start with a frequency band of 2–5 Hz and increase the bandwidth in steps of 1 Hz up to 2–10 Hz. The small steps of 1 Hz proved to be more stable than using a larger increment.

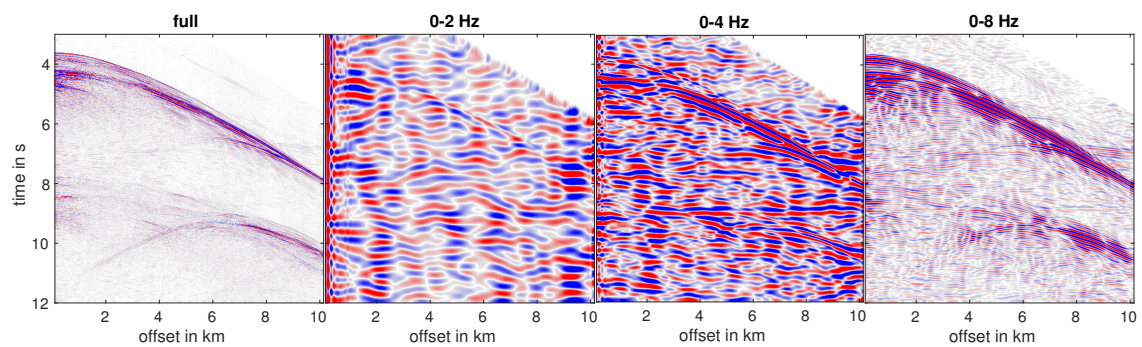
All FWI results shown in this paper present the final inversion result after convergence. The convergence is reached if the inversion can no longer reduce the relative misfit by more than 1%. As a consequence, inversion results can differ in the number of performed iterations. Please also note that in order to be able to evaluate the differences in the results as best as possible, the number of inverted parameters was kept as low as possible. Therefore, the acoustic inversion only includes the density and P-wave velocity, whereas the elastic inversion additionally includes the S-wave velocity. However, further parameters such as attenuation and anisotropy were not inverted. These parameters also influence the elastic and acoustic FWI results but are not discussed in detail in this work.

DATA AND MODEL

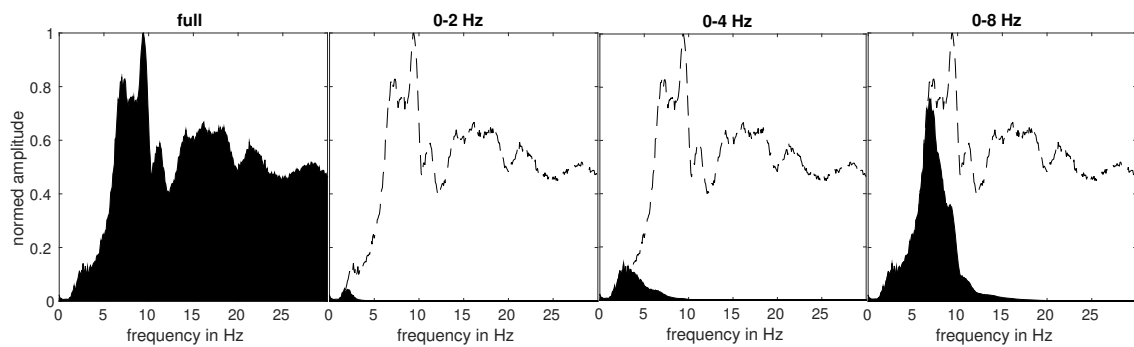
The data set used in this work was provided by Petroleum Geo-Services (PGS). It was acquired offshore Angola, West Africa using a 2D single-streamer acquisition geometry. The source depth was 8 m, the dual-sensor streamer depth was 20 m, the distance from the centre of the source to the centre of the first hydrophone group was 100 m, and the streamer had a total length of about 10 km. A hydrophone distance of 12.5 m results in 804 receivers per shot. The subset of the data used here covers a profile length of 20 km and uses 19 shots with a recording length of 12 s and a shot distance of 500 m. Thiel (2018) investigated the impact of the shot decimation on FWI results; the setup chosen here turned out to be the best compromise between quality of the results and computational cost. The data were already wavefield-separated (Amundsen, 1993; Klüver, 2008), i.e., the upgoing wavefield without receiver ghost is used in this work. Useful signal in the data can be observed starting at around 3–4 Hz. Figure 1 shows an exemplary shot gather (full offset range) and various filter panels. Each filter panel adds one octave. All shot gathers typically exhibit quite complex event patterns with diffraction-like events appearing and disappearing along the line, often caused by the salt structure with its strong topology.

In addition to the seismic prestack data, we were provided with a P-wave velocity model optimised by migration velocity analysis (Figure II), and the associated final Kirchhoff migration result (a zoom is shown in Figure II). In the migration result, several distinct layers in the sediments above the salt are visible. Therefore, we expect similarly shaped updates in the inversion results. The initial parameter models for all inversions are shown in Figure 2, left column. The P-wave subsurface model (Figure II) is composed of a 3 km water column ($v_P = 1490$ m/s; white colour), followed by sediments with increasing velocities (gradient; blue colour to orange colour). Inside the sediments, a continuous salt structure (4500 m/s; red colour) of up to 4 km thickness with complex topology and varying thickness is included. The S-wave model (Figure II) and the density model (Figure II) were obtained by applying an empirical relation after Gardner et al. (1974) and v_P/v_S -ratios from literature (Bourbié et al., 1987). The stars at the surface denote the shots used in the inversions. Receivers are located to the left of each shot, i.e., the vessel's movement was from left to right. These models do not only serve as starting models in all inversions but the smooth P-wave model was also used for the final migration.

Figure 2, right column, shows the models used to generate data for synthetic tests. As opposed to the starting models, these models contain a rather prominent, distinct layer in the sediments above the salt, based on interpretation of the structural image. The high-velocity layer is about 100 m thick, i.e., the



(a) Filtered data in the time domain for different low-pass filters. The data were normalised to the maximum amplitude of the near-offset trace.



(b) Frequency content of the low-pass filtered data (black area) in comparison to the full frequency content (dashed line).

Figure 1: Exemplary shot gather plotted in the time and frequency domain, filtered with different corner frequencies. Each filter panel adds one octave. The data were filtered with a 6th-order low-pass Butterworth filter with the cutoff frequency given in the title of each panel.

thickness of the additional layer equals about half the wavelength for the maximum frequency of 10 Hz considered in the inversion later on. Due to the relatively strong velocity contrast, the layer adds another strong reflectivity feature to the model. The density and S-wave velocity models shown in Figure II and II, respectively, were updated accordingly as outlined above. One goal of the synthetic inversion tests is to determine the ability of FWI to find this structure.

FORWARD MODELLING TESTS

In order to study the influence of elastic properties of the model, in particular mode conversions, we calculated acoustically and elastically forward-modelled wavefields. The wavefields were propagated in the initial models shown in Figure 2, left column. Snapshots for an exemplary shot, taken at time $t = 4.44$ s, are displayed in Figure 3. For better orientation, the sea floor and the TOS, picked from the migrated image, are displayed as black lines. To ensure comparability, all snapshots are scaled equally. The upper two plots (Figure II and II) show the energy of the compressional waves of the acoustically and elastically modelled wavefields, respectively. Figure II shows their difference. The S-wave energy, plotted in Figure II, is obviously only available in elastic modelling and zero for acoustic modelling (hence not displayed).

The difference plot shows the discrepancy in P-wave energy for acoustic and elastic modelling. Since water is assumed purely acoustic, the direct wave is identical in both the acoustic and elastic simulation, i.e., the direct wave is not visible in the difference plot. Also, the reflection of the sea floor is hardly visible in the difference plot as only little energy is converted into S-waves. Most of the differences appear in the reflection from the TOS (annotated as salt reflection in Figure II), i.e., significant energy is mode-converted when hitting the TOS. From the high amplitudes in the difference plot we conclude that elastic effects in the presence of salt are significant, even for towed-streamer data where only pressure changes are recorded by hydrophones in the water column. The effect does not reveal itself as additional events that get recorded by the hydrophones. By comparing the wavefield snapshots it can be observed that the main part of the converted energy is trapped in the sediments between the sea floor and the TOS, or transmitted into the salt layer. Therefore, the main differences in the recorded wavefields at the surface are the changes of relative amplitudes of events. This can be observed in particular for the salt reflection and the diffractions from the top of salt (see Figure II). Consequently, we expect that acoustic FWI will not be able to fit the amplitudes of forward modelled data and field data correctly even within one trace, normalised or not.

INVERSION TESTS

In order to check the FWI performance that can be expected for the given model and acquisition geometry, a synthetic test was conducted prior to starting any field data inversion. The synthetic reference data used as input for the inversion were simulated using elastic forward modelling in the models shown on the right-hand side of Figure 2, i.e., the models including the thin high-velocity layer in the sediments, indicated by the migration result. The acquisition geometry was based on the actual geometry of the field data, and we added 10 % of random noise to the simulated seismograms. Actual field data often also contain coherent noise; such noise should be removed or attenuated as best as possible prior to running FWI unless it can be modelled with sufficient accuracy. As starting models for FWI, the models without the high-reflectivity layer in the sediments were used. The inversion started in a frequency band of 2–5 Hz. The bandwidth was increased in steps of 1 Hz after a minimum of 8 iterations until 2–10 Hz was reached.

The results of the acoustic and elastic inversions are displayed in Figure 4. The inversion results of the input data show no considerable updates in the left part of the model between 0–5 km. This is caused by the acquisition geometry and shot selection, as the shots are located only in the right half of the model and no waves recorded at the corresponding streamer locations travelled through that part of the model. In the acoustic results (left column) for model coordinates $x = 15$ –20 km, the inversion increased the velocity and density at the location of the high-contrast layer in the sediments. The actual density values of the distinct layer are overestimated by up to 20 %. In the central part, no such layer is visible due to various artefacts. The artefacts in the density model exhibit large contrasts of up to 1500 kg/m³ within a range of just 100 m and obscure all updates of the sediment layers. The same happens in the velocity result. In other words, the results are unreliable.

In the elastic inversion results the high-contrast layer is outlined considerably better. Apart from the left side as mentioned above, the layer is visible over the full horizontal dimension of the model. The actual

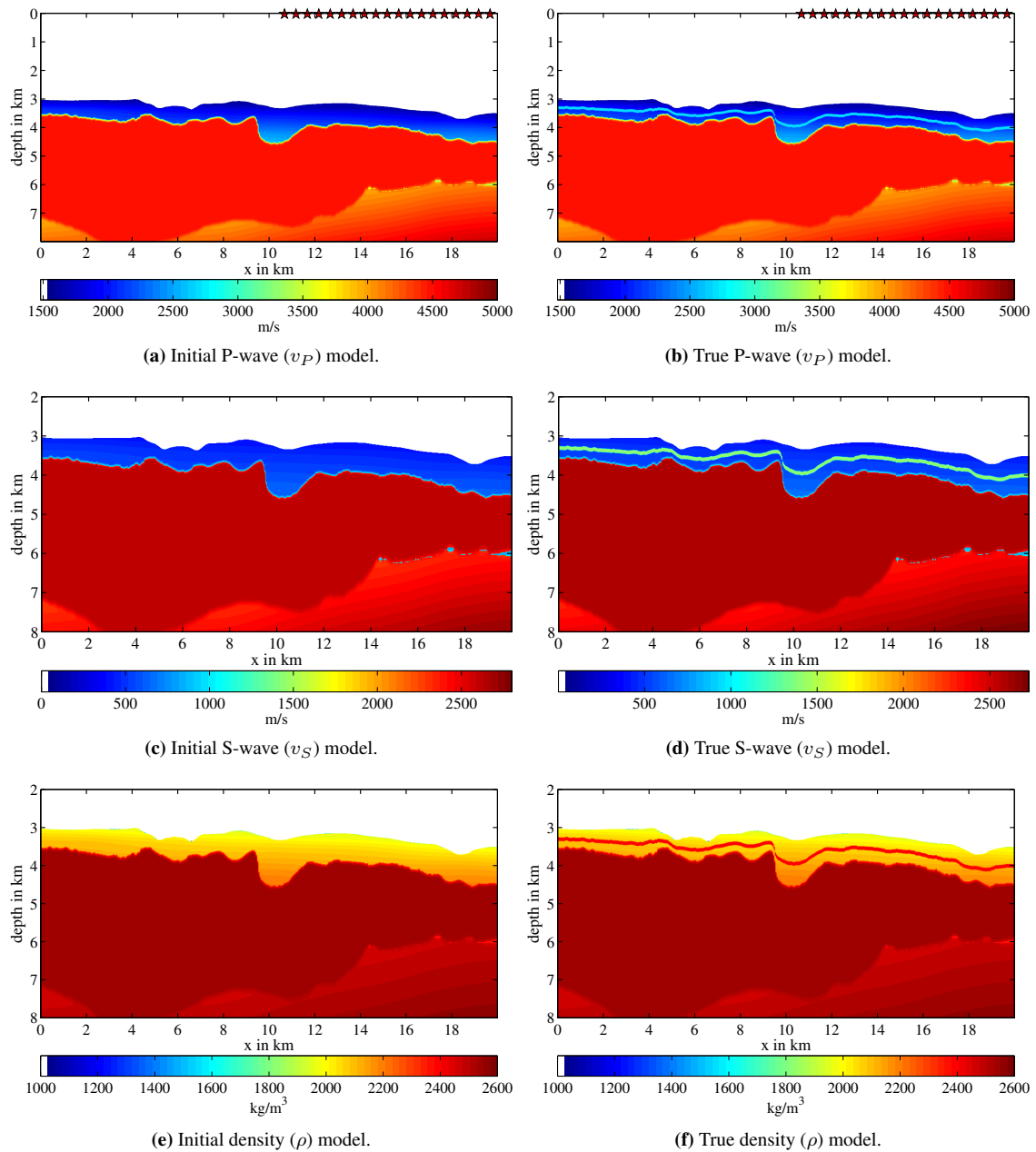
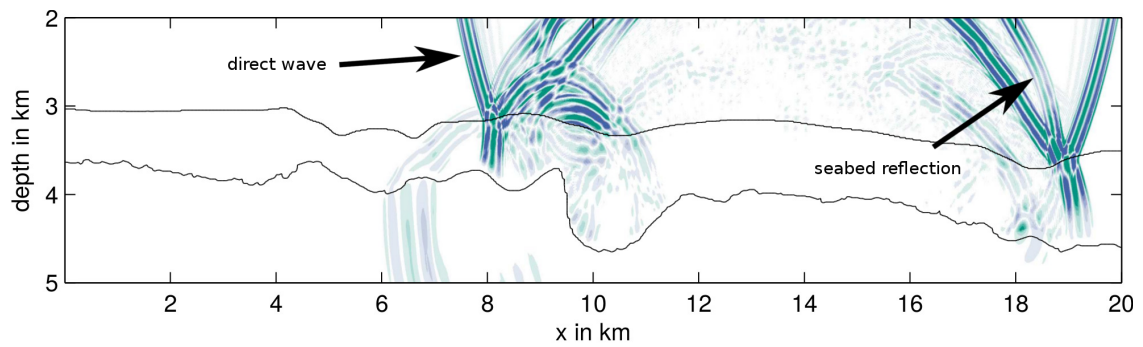
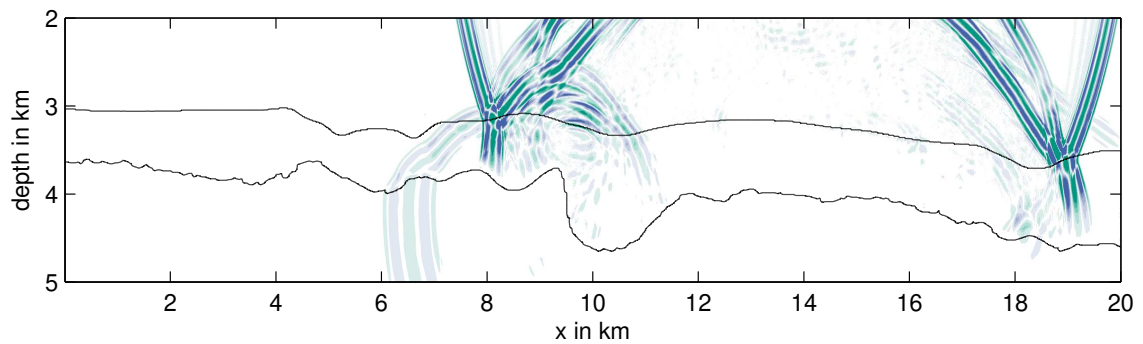


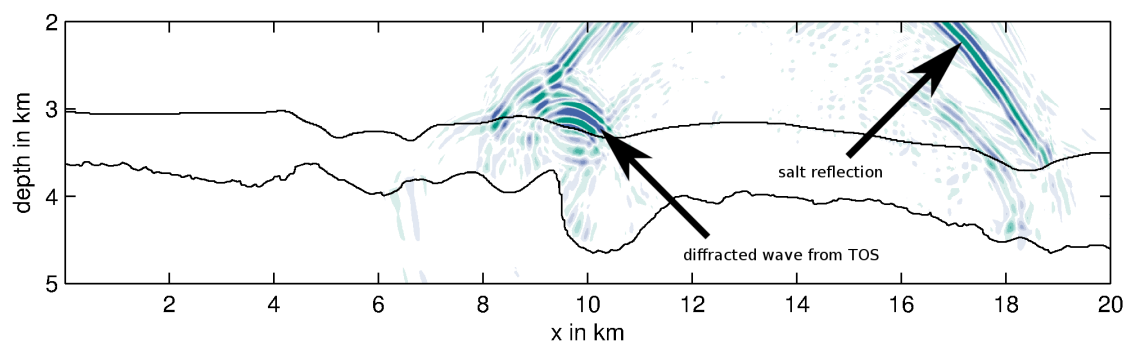
Figure 2: Initial models (left column) and models used to generate synthetic data (right column) for various tests shown in this work. The initial models serve as starting models for all inversions; the initial P-wave velocity model was used for Kirchhoff migration. Stars denote shot positions used for inversion tests. The salt structure with its complex topology is clearly visible in all parameter models.



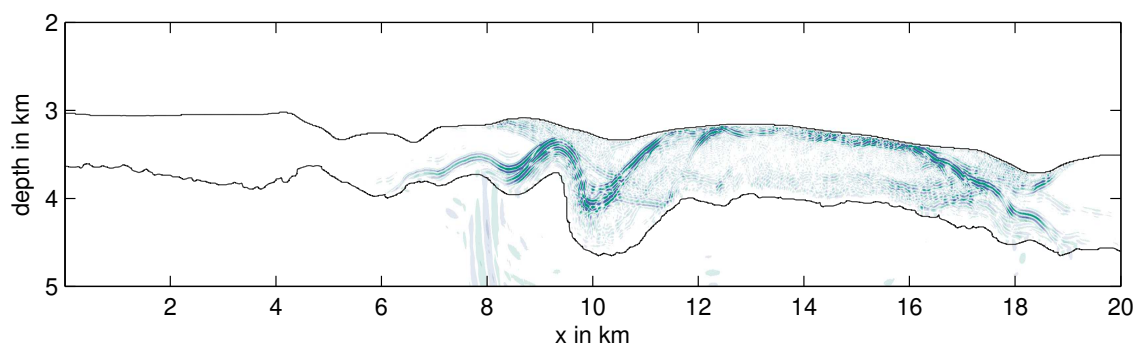
(a) Energy in compressional waves, acoustic forward modelling.



(b) Energy in compressional waves, elastic forward modelling.



(c) Difference of acoustic and elastic compressional energy.



(d) Energy in shear waves, elastic forward modelling.

Figure 3: Comparison of acoustic and elastic forward-modelled wavefields. Snapshots of the forward-simulated wavefield in the initial model shown in Figure 2, left column, at $t = 4.44$ s. The first contour line in black represents the sea floor reflector, the second contour line is the top of salt. All amplitudes are normalised equally.

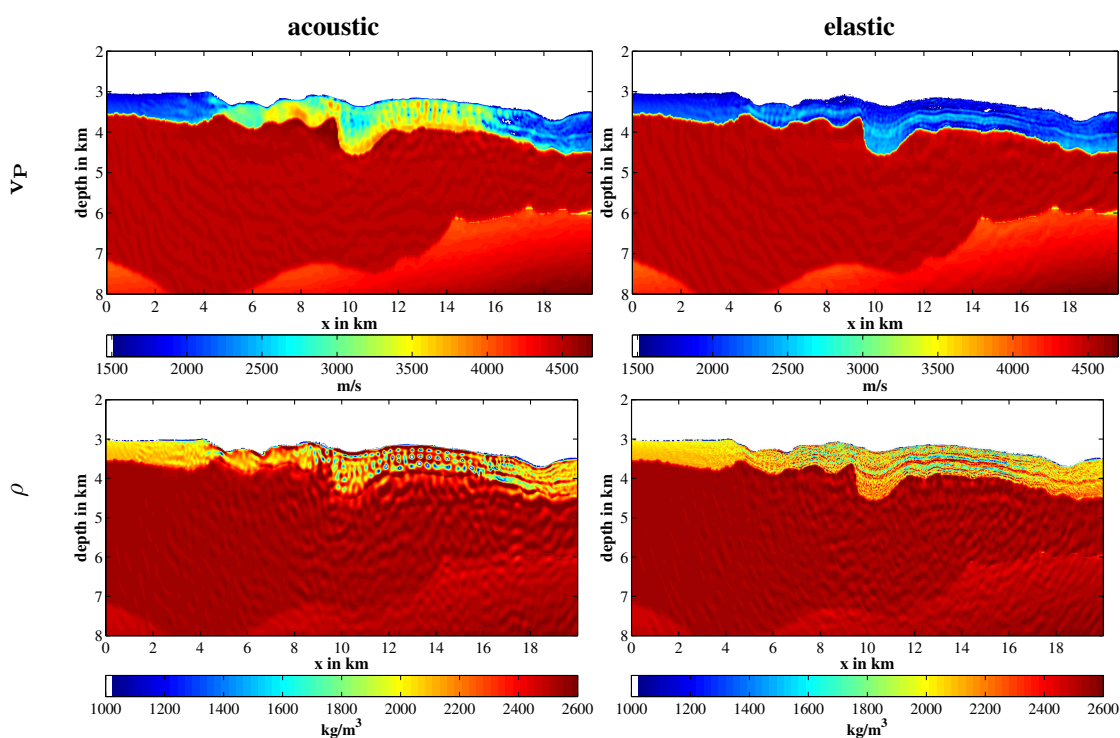


Figure 4: Synthetic inversion test up to 10 Hz. Left column: acoustic inversion of P-wave velocity v_P and density ρ ; right column: the corresponding elastic inversion results.

values of the layer were fitted much better and are no longer overestimated. Noise is visible as small-scale artefacts, appearing in most areas of the model, but significantly reduced compared to the acoustic case. In contrast to the density and P-wave velocity updates, the updates of the S-wave velocity (not shown here) are only weak. The reason for this is that almost no energy from converted S-waves is converted back to P-waves at the sea floor and then propagating through the water layer towards the surface which can be verified by looking at the divergence and curl wavefields, representing the P-wave part and S-wave part of the full wavefield. The main effect of the elastic reconstruction is on amplitudes, i.e., the loss in P-wave energy due to mode conversions is taken much better into account, as expected.

FIELD DATA INVERSIONS

In the following, we are going to compare FWI inversion results for both the acoustic and elastic approach. Obviously, given different starting models, different modelling engines, different inversion schemes, and, in general, being able to fit different parts of the total wavefield using the two approaches, it is not easy to run a fair comparison. As outlined earlier, we have chosen to let each individual inversion meet the convergence criterion, i.e., the data misfit in the corresponding inversion could no longer be reduced in a significant way. As a consequence, the final number of iterations specified below differs between both approaches.

Acoustic FWI

The results of the acoustic field data inversion are shown in Figure II-II. The same starting models as used for the synthetic tests (see Figure 2) were utilised here. The inversion of the v_P parameter updated only long-wavelength structures in the sediments above the salt. There is, apart from the rightmost part of the inversion result, no distinct high-velocity layer visible. The density model shows some more detail but in general all updates appear blocky and are clearly dominated by artefacts. Also, the introduced contrasts are very high with, for instance in some parts of the inverted density model, a change of almost 1000 kg/m^3

within a few hundred metres. This was already observed in the synthetic example and can be explained by the acoustic inversion trying to fit amplitudes using data with elastic effects. Due to the good starting model optimised by migration velocity analysis and the availability of fairly low-frequency data, cycle-skipping was no major issue, at least for the region of interest up to the salt body itself. The acoustic inversion was able to reduce the initial data misfit by only 22 % in 60 iterations, up to aforementioned frequency of 10 Hz. No further improvements could be achieved even when higher frequencies were included or more iterations were run. The misfit remained high as the inversion was unable to find consistent model updates.

The data fit for three exemplary traces with varying offset from shot 7 is plotted in Figure II. The field data are displayed in black while the forward-modelled data using the final inverted parameter models are shown in red. Some of the main events could be fitted but, in general, many events do not match, neither in phase nor in amplitude. The same can be seen by comparing the field data and the modelled shot gather using the inverted parameter models, see Figures II and II. Only the main features match and there are clear amplitude differences that can already be seen visually. A comparison of the STF inversion results (Figure II) also exhibits inconsistencies, especially in the central part of the utilised shot range. These differences indicate insufficiencies in the model and/or the modelling approach. For marine data and sufficiently accurate parameter models, we would expect the inverted STFs to match fairly well over the entire survey. Clearly, the acoustic FWI approach did not work very well in this case.

Elastic FWI

The results of the elastic inversion after 89 iterations (up to 10 Hz) of v_P and ρ are shown in Figure II-II. Due to the low sensitivity of S-wave velocity in the given streamer acquisition geometry the reconstructed v_S models suffer strongly from noise in the field data (Thiel, 2018). Reconstructions of v_S are therefore not shown. While we expect certain cross-talk between the parameters, the inversion has in general worked much better than the acoustic inversion with fewer artefacts. In particular the density parameter shows remarkable details. Some small-scale vertical artefacts are visible, caused by the acquisition geometry. After 89 iterations the inversion was able to reduce the initial data misfit by almost 60 %.

In order to check the results, we show the same four additional plots as before: The data fit for the three traces from shot 7 is plotted in Figure II, the STF inversion results are displayed in Figure II, and the comparison of the field data and the modelled data using the final inverted parameter models are shown in Figure II and II, respectively. We again display the field data in black and the forward-modelled data in red. This time, the main events could be fitted in phase and amplitude, at least up to a certain traveltimes which includes our region of interest, namely the sediments and upper part of the salt body. The STF inversion results show a much more consistent behaviour for all shots. No phase changes can be observed, only small unconformities are visible for the central shots (shot 8-12). These unconformities can be traced back to small errors in the location of the deep syncline in the salt between $x = 9-11$ km and the syncline above in the seafloor. Due to the shallow location and strong contrast, also small location errors are mapped into the inverted source wavelet.

The modelled data represent the field data much better than in the acoustic case. The overall amplitude balance has clearly improved. The mid-offset range still has higher amplitudes in the field data compared to the modelled data, though.

Direct comparison

Figure 7 shows zoomed sections of the v_P and ρ results of both the acoustic and elastic full-waveform inversion. For comparison, a Kirchhoff migration result using the full frequency content of the data and the starting P-wave velocity model shown in Figure II is also plotted. Both density models were smoothed with a horizontal Gaussian filter in order to decrease small-scale artefacts. Exemplary structures were picked in the migration result and plotted as black lines over the FWI results. The location of the structures in the FWI result does not necessarily have to match exactly with the migration result because the Kirchhoff migration used the starting model for calculating traveltimes. In other words, the black lines should only be seen as guidance. It should be noted that the initial velocity starting model for FWI represents the long-wavelength features quite accurately. Events in common-image gathers (CIGs) are therefore already fairly flat using the starting model, in particular above the salt where the focus of this work lies. Although the

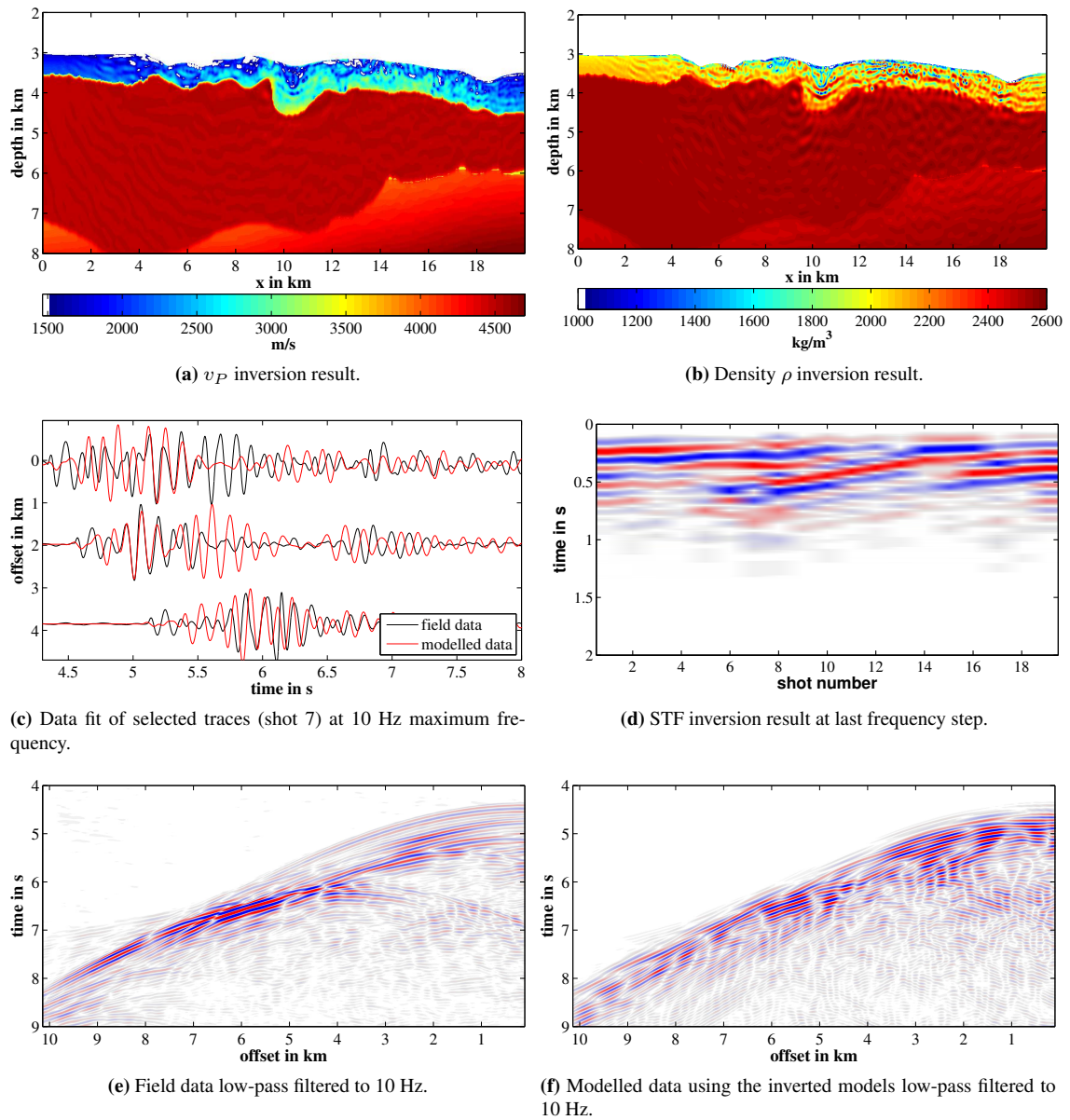


Figure 5: Acoustic inversion results after 60 iterations, using the starting models shown in Figure 2 (left).

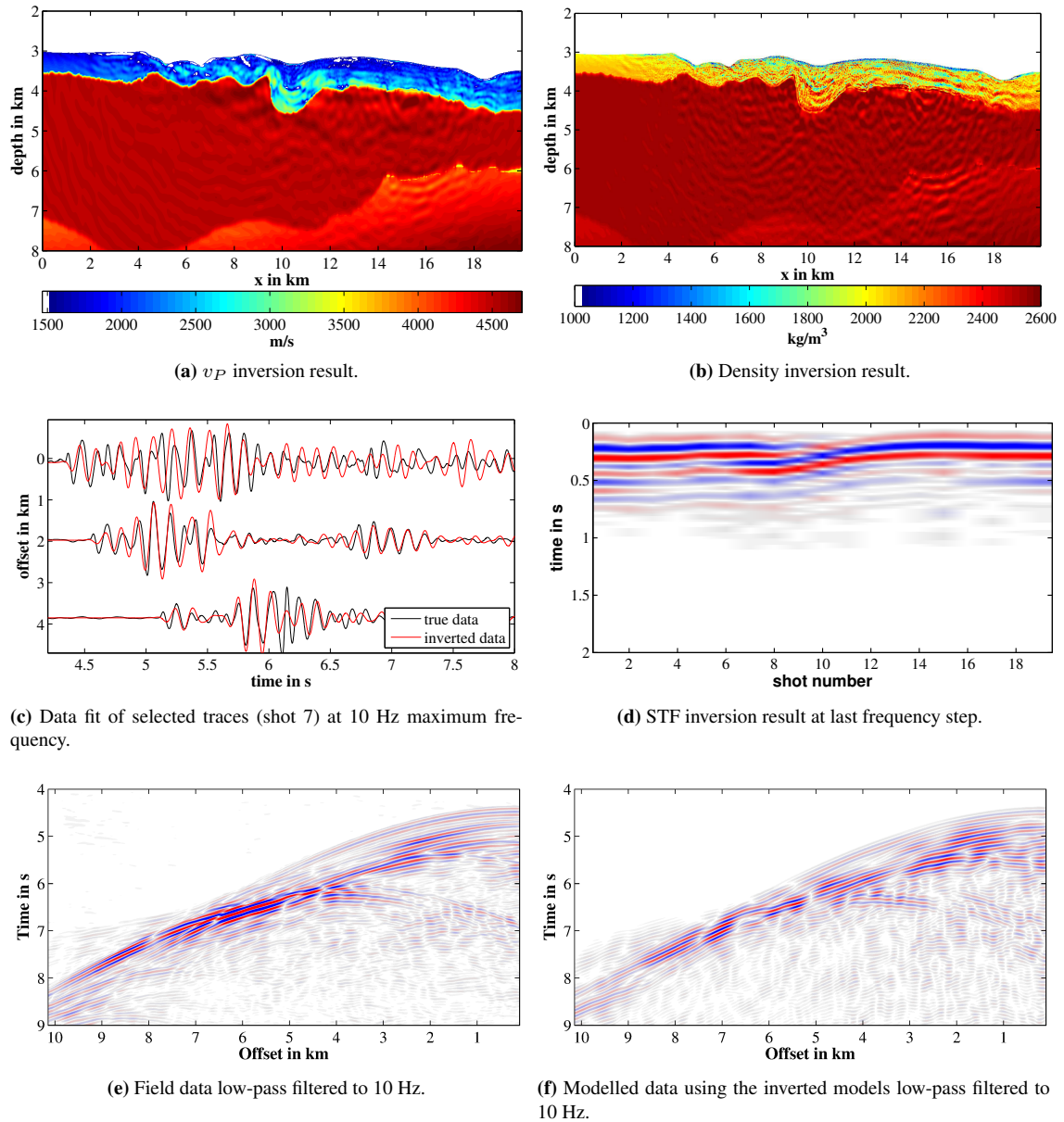


Figure 6: Elastic inversion results after 89 iterations, using the starting models shown in Figure 2 (left).

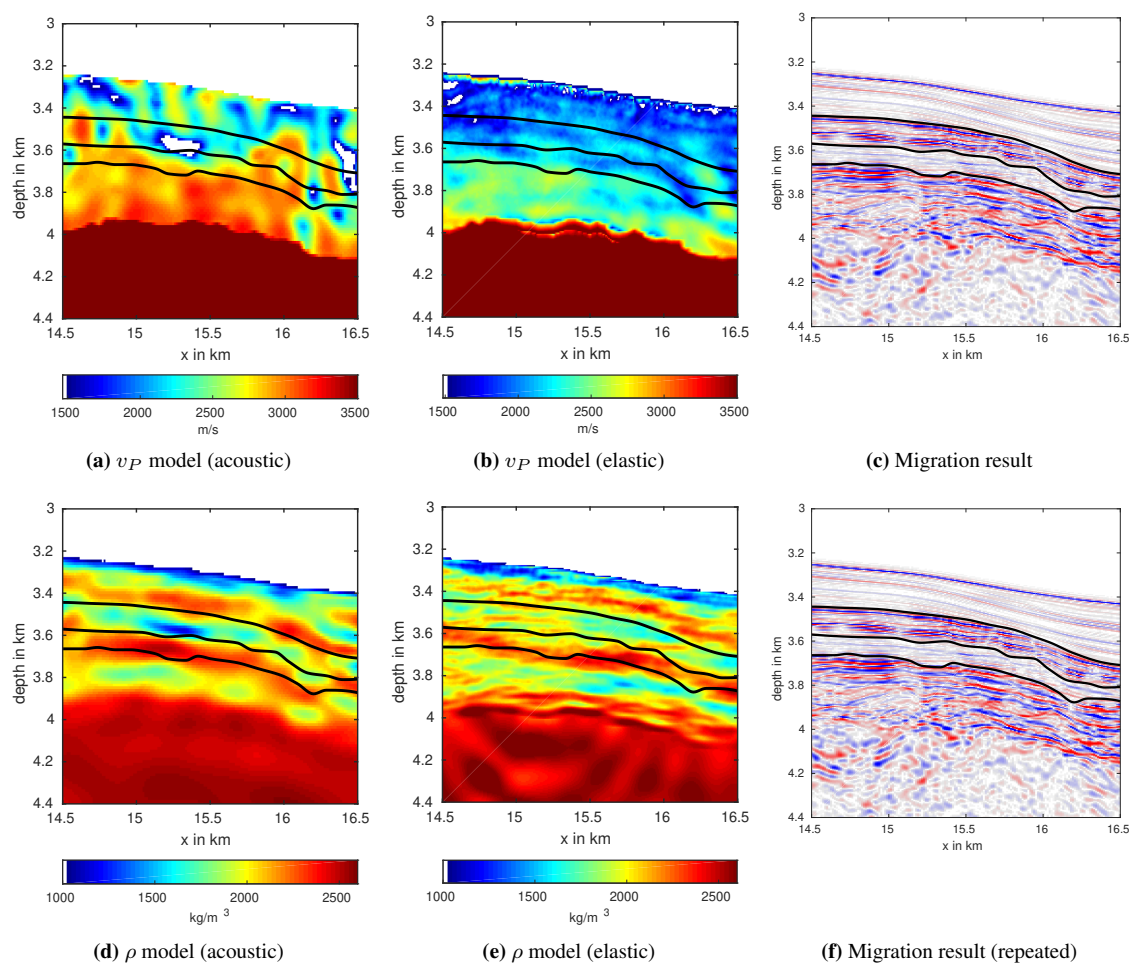


Figure 7: Zoom of the acoustically and elastically inverted v_P (a and b) and density ρ (d and e) models, respectively. For comparison, a Kirchhoff migration result obtained with the starting model shown in Figure II is shown (c; repeated in f). Exemplary structures were picked in the migration result and plotted as black lines over the FWI results. Please note that the color bar in (a) and (b) has a smaller range compared to the previous v_P figures to better highlight the structures.

models inverted by FWI show much more detail, the migration result itself and the flatness of events in CIGs do not change much in the area above the salt, even when a more sophisticated migration engine than Kirchhoff migration is used. This phenomenon is well known, see, for instance, Allemand and Lambaré (2015) for details.

The elastic FWI process has started to build up the high-contrast layer in the sediments, clearly visible in the migration result. The layer was completely missing in the initial parameter models (see Figure 2, left side) and hardly visible in the acoustic inversion. Especially the v_P result improved considerably for the elastic inversion. We believe that the large-scale features extending over a few kilometers are reliable, whereas small-scale structures might be caused by insufficiency of assumed physics such as geometrical spreading. The picked lines can be linked to inverted laterally extended structures in the sediments, which was not possible in the acoustic v_P result. All in all, in comparison to the acoustic results the elastic inversion shows a more reliable image of large-scale subsurface structures.

ATTENUATION

For all inversion results, no attenuation was included. Generally, the effect of attenuation of P-waves in our model is small and in the water column and the salt body the attenuation can be neglected. The number of P-wavelengths propagating in the sediments (average thickness below 1 km) is below 15 (see snapshots of Figure 3). The small loss of amplitude with increasing frequency (low-pass filter) in the sediments can, therefore, be mostly compensated by the Wiener filter STF inversion (see Groos, 2013). The influence of velocity dispersion on the P-wave phases is also expected to be negligible in our case due to the small number of wavelengths propagating in the sediments and the generally small velocity dispersion caused by attenuation: at $Q = 50$ the velocity dispersion is significantly below 1%. To be sure we also ran reconstruction tests (not shown here) where we included attenuation in the sediments and found no relevant effect on the reconstructed velocity model.

CONCLUSIONS

In this work we presented the application of acoustic and elastic FWI to 2D marine towed-streamer field data acquired over a salt structure. It turned out that such data, which would traditionally be processed using an acoustic approximation, required an elastic FWI approach to produce reasonable parameter models and detect structures in the sediments that were otherwise obscured by artefacts. FWI has potential to enhance older 2D legacy data sets only processed with standard ray-based methods; we can gain more information about the subsurface provided low frequencies, sufficiently accurate starting models and/or techniques to overcome cycle-skipping are available. Further improvements of the results may be obtained by including anisotropy and/or attenuation in the modelling and possibly the inversion, but additional constraints might be necessary in order to do so. Especially sediments are often affected by anisotropic characteristics. Nevertheless, even assuming an isotropic elastic medium without attenuation, the inversion was able to image all main structures in the density and v_P models. We recommend to carefully check on the existence of elastic effects also for marine-towed streamer data before deciding on the processing and imaging strategy for FWI.

ACKNOWLEDGMENTS

We thank Petroleum Geo-Services for providing the data set and starting velocity model, and for interesting discussions regarding data interpretation. This work was kindly supported by the sponsors of the Wave Inversion Technology (WIT) consortium. We gratefully acknowledge financial support by the Deutsche Forschungsgemeinschaft (DFG) through CRC 1173. The computations were performed on the supercomputer ForHLR II at the Steinbuch Centre for Computing, Karlsruhe Institute of Technology.

PUBLICATION

This WIT article was submitted for publication in *Geophysical Prospecting*.

REFERENCES

- Allemand, T. and Lambaré, G. (2015). Combining Full Waveform Inversion and Tomography: Full Waveform Inversion-guided Tomography. In *77th Conference & Exhibition Extended Abstracts*. European Association of Geoscientists & Engineers.
- Amundsen, L. (1993). Wavenumber-based filtering of marine point-source data. *Geophysics*, 58(9):1335–1348.
- Bohlen, T. (2002). Parallel 3-D viscoelastic finite difference seismic modelling. *Computers & Geosciences*, 28(8):887–899.
- Bourbié, T., Coussy, O., and Zinszner, B. (1987). *Acoustics of porous media*. Institut Français du Pétrole publications. AFD. Technip, Paris.
- Brossier, R., Operto, S., and Virieux, J. (2009). Seismic imaging of complex onshore structures by 2D elastic frequency-domain full-waveform inversion. *Geophysics*, 74(6):WCC105–WCC118.

- Bunks, C., Saleck, F. M., Zaleski, S., and Chavent, G. (1995). Multiscale seismic waveform inversion. *Geophysics*, 60(5):1457–1473.
- Choi, Y. and Alkhalifah, T. (2012). Application of multi-source waveform inversion to marine streamer data using the global correlation norm. *Geophysical Prospecting*, 60:748–758.
- Forbriger, T., Groos, L., and Schäfer, M. (2014). Line-source simulation for shallow-seismic data. Part 1: Theoretical background. *Geophysical Journal International*, 198(3):1387–1404.
- Gardner, G. H. F., Gardner, L. W., and Gregory, A. R. (1974). Formation Basics for Velocity and Density - The Traps Diagnostic Stratigraphic. *Geophysics*, 39(6):770–780.
- Groos, L. (2013). *2D full waveform inversion of shallow seismic Rayleigh waves*. PhD thesis, Karlsruhe, Karlsruher Institut für Technologie (KIT), Diss., 2013.
- Jeong, W., Lee, H.-Y., and Min, D.-J. (2012). Full waveform inversion strategy for density in the frequency domain. *Geophysical Journal International*, 188(3):1221–1242.
- Klüver, T. (2008). Wavefield separation for dual-sensor data with local handling of aliased energy. In *Technical Program Expanded Abstracts*. Society of Exploration Geophysicists.
- Köhn, D. (2011). *Time Domain 2D Elastic Full Waveform Tomography*. PhD thesis, Christian-Albrechts-Universität zu Kiel.
- Köhn, D., De Nil, D., Kurzmann, A., Przebindowska, A., and Bohlen, T. (2012). On the influence of model parametrization in elastic full waveform tomography. *Geophysical Journal International*, 191(1):325–345.
- Komatitsch, D. and Martin, R. (2007). An unsplit convolutional perfectly matched layer improved at grazing incidence for the seismic wave equation. *Geophysics*, 72(5):SM155–SM167.
- Levander, A. R. (1988). Fourth-order finite-difference P-SV seismograms. *Geophysics*, 53(11):1425–1436.
- Lu, R., Lazaratos, S., Wang, K., Cha, Y., Chikichev, I., and Prosser, R. (2013). High-resolution elastic FWI for reservoir characterization. In *75th Conference & Exhibition Extended Abstracts*. European Association of Geoscientists & Engineers.
- Martin, R. and Komatitsch, D. (2009). An unsplit convolutional perfectly matched layer technique improved at grazing incidence for the viscoelastic wave equation. *Geophysical Journal International*, 179(1):333–344.
- Mora, P. (1987). Nonlinear two-dimensional elastic inversion of multioffset seismic data. *Geophysics*, 52(9):1211–1228.
- Nocedal, J. and Wright, S. (1999). Numerical optimization. *Springer Science*, 35:67–68.
- Plessix, R.-E. (2006). A review of the adjoint-state method for computing the gradient of a functional with geophysical applications. *Geophysical Journal International*, 167(2):495–503.
- Plessix, R.-E., Milcik, P., Rynja, H., Stopin, A., Matson, K., and Abri, S. (2013). Multiparameter full-waveform inversion: Marine and land examples. *The Leading Edge*, 32(9):1030–1038.
- Pratt, R. G. (1999). Seismic waveform inversion in the frequency domain, Part 1: Theory and verification in a physical scale model. *Geophysics*, 64(3):888–901.
- Przebindowska, A. (2013). *Acoustic full waveform inversion of marine reflection seismic data*. PhD thesis, Karlsruhe Institute of Technology (KIT).
- Robertsson, J. O., Levander, A., Symes, W. W., and Holliger, K. (1995). A comparative study of free-surface boundary conditions for finite-difference simulation of elastic/viscoelastic wave propagation. In *Technical Program Expanded Abstracts*, pages 1277–1280. Society of Exploration Geophysicists.

- Shipp, R. M. and Singh, S. C. (2002). Two-dimensional full wavefield inversion of wide-aperture marine seismic streamer data. *Geophysical Journal International*, 151(2):325–344.
- Tarantola, A. (1984). Inversion of seismic reflection data in the acoustic approximation. *Geophysics*, 49(8):1259–1266.
- Thiel, N. (2018). *Acoustic and elastic FWI of marine dual-sensor streamer data in the presence of salt*. PhD thesis, Karlsruher Institut für Technologie (KIT).
- Tromp, J., Tape, C., and Liu, Q. (2005). Seismic tomography, adjoint methods, time reversal and banana-doughnut kernels. *Geophysical Journal International*, 160(1):195–216.
- Vigh, D., Jiao, K., Watts, D., and Sun, D. (2014). Elastic full-waveform inversion application using multi-component measurements of seismic data collection. *Geophysics*, 79(2):R63–R77.
- Virieux, J. (1986). P-SV wave propagation in heterogeneous media: Velocity-stress finite-difference method. *Geophysics*, 51(4):889–901.
- Warner, M., Ratcliffe, A., Nangoo, T., Morgan, J., Umpleby, A., Shah, N., Vinje, V., Štekl, I., Guasch, L., Win, C., Conroy, G., and Bertrand, A. (2013). Anisotropic 3D full-waveform inversion. *Geophysics*, 78(2):R59–R80.
- Xiao, B., Kotova, N., Bretherton, S., Ratcliffe, A., Duval, G., Page, C., and Pape, O. (2016). An offshore Gabon full-waveform inversion case study. *Interpretation*, 4(4).